Railway wheel tread damage and axle bending stress – Instrumented wheelset measurements and numerical simulations

N.B. When citing this work, cite the original published paper.

(article starts on next page)

Railway wheel tread damage and axle bending stress – Instrumented wheelset measurements and numerical simulations

Michele Maglio, Tore Vernersson, Jens C O Nielsen, Astrid Pieringer, Pär Söderström, Daniele Regazzi & Steven Cervello

Published online: 07 Jun 2021.

Submit your article to this journal ↗

Article views: 69

View related articles ↗

View Crossmark data ↗

Railway wheel tread damage and axle bending stress – Instrumented wheelset measurements and numerical simulations

Michele Maglio[a], Tore Vernersson[a], Jens C O Nielsen[a], Astrid Pieringer[b], Pär Söderström[c], Daniele Regazzi[d] and Steven Cervello[d]

[a]CHARMEC, Division of Dynamics, Department of Mechanical and Maritime Sciences, Chalmers University of Technology, Gothenburg, Sweden; [b]CHARMEC, Division of Applied Acoustics, Department of Architecture and Civil Engineering, Chalmers University of Technology, Gothenburg, Sweden; [c]SJ AB, Rolling Stock Division, Stockholm, Sweden; [d]Lucchini RS, Railway Division, Lovere, Italy

ABSTRACT

A combination of instrumented wheelset measurements and numerical simulations of axle bending stresses is used to investigate the consequences of evolving rolling contact fatigue (RCF) damage on a passenger train wheelset. In a field test campaign, stresses have been monitored using a wheelset with four strain gauges mounted on the axle, while the evolution of wheel tread damage (out-of-roundness) has been measured on regular occasions. The strain signals are post-processed in real time and stress variations are computed. Based on a convolution integral approach, the measured wheel out-of-roundness has been used as input to numerical simulations of vertical dynamic wheelset–track interaction and axle stresses. Simulated and measured axle stresses are compared for cases involving combinations of low or high levels of rail roughness and the measured levels of RCF damage. The study enhances the understanding of how wheel tread damage and track quality influence axle stress amplitudes.

1. Introduction

Railway axles are critical components of the vehicle running gear. Their correct functioning is particularly important with respect to travel safety. Since the 'Versailles accident', which occurred in 1842, axle design procedures have gradually improved [1]. Today, the probability of axle fractures per train kilometre in the European Union is extremely low. For example, from 2006 to 2009 there was only one fracture event per 50.45 millions of train kilometres [2]. Nevertheless, if an axle fracture does occur it can have catastrophic consequences. In the Viareggio (Italy) accident in 2009, the sudden failure of the leading axle of the first waggon caused the derailment of a freight train carrying liquefied petroleum gas (LPG) [1]. Two of the waggons exploded and 32 people lost their lives due to the incident [3].

In Europe, axle design is currently regulated by the standard EN 13103–1 [4] (for axles with external journals). The calculations in this standard are based on static design loads acting on the wheelset. Magnification factors are employed to account for dynamic loads (e.g. due to the effects of irregularities in track geometry and stiffness, braking, curving, traction, and switches & crossings). Fatigue stresses are calculated at different sections of the axle (based on the axle geometry, information on vehicle dimensions, operating conditions and braking or traction system) and comparisons can be made with allowed stress levels for specific axle steel grades at specified axle zones. In this standard, the employed design loads are independent of the actual train operating conditions. For instance, the excitation of wheelset dynamics because of tread damage and out-of-round wheels is not accounted for.

The approach adopted in the standard is supposed to completely prevent crack initiation in axles from occurring. However, cracks could still be initiated at locations where damage and/or corrosion pits could grow during service. In order to detect cracks before they reach a critical length, axles are inspected at regular intervals [5]. Non-destructive testing (NDT) in the form of ultrasonic testing is the most common inspection technique for axles. NDT is based on the hypothesis that flaws of a certain size can be detected with an expectancy rate referred to as the probability of detection (POD) [6]. For passenger trains, such tests are performed according to the European standard EN 15313 [7].

Traditionally, the inspections of train wheelsets are scheduled depending on the mileage covered by the vehicle. However, a more flexible planning of the maintenance could reduce overall maintenance costs by avoiding non-necessary replacements of components, but also increase the availability of the fleet. Indeed, many operators are currently aiming at optimizing their maintenance intervals according to the observed conditions of their assets [8]. This strategy is referred to as condition-based maintenance [9]. As an example, information on the status of a wheelset can be collected by the monitoring of bending and torsion stresses at critical sections of the axle [8], or by measuring the dynamic loads generated by the wheelset when passing over wayside wheel impact load detectors (WILDs) [10]. Further, information regarding the temperature and vibrations in railway bearings can be monitored in real time using wireless equipment [11]. In this way, maintenance can be postponed as long as the monitored parameters are within the 'safe' range, which is determined by regulations or by an assessment according to company practises.

Condition-based wheelset maintenance can be enhanced by improving the understanding of the influence of different forms of running surface damage on wheel treads and rail heads on component fatigue life. This can be investigated using field measurements. For example, wheel–rail contact forces and axle stresses can be measured using instrumented wheelsets with strain gauges mounted on the axle body or on the wheel web [12]. In an investigation of the influence of rail corrugation on high-frequency vertical wheel–rail contact forces, the leading wheelset of a Swedish high-speed train was equipped with strain gauges on the wheel webs [13]. The results showed that dynamic forces in the frequency range 100–1250 Hz, generated by short-pitch rail corrugation, contributed to the development of RCF on the wheels.

In this paper, the consequences of evolving wheel tread damage and wheel out-of-roundness (OOR) are studied by means of both field measurements and simulations. For

a given train route, the effect of evolving tread damage on the amplitude spectrum of measured axle stresses is investigated. The influences of variations in operational parameters, such as track quality and the angular positions of the sensors, are also studied. In a field test campaign, which started in January 2019, axle bending stresses have been measured using an instrumented powered wheelset mounted on a regional train in Sweden. For this purpose, the wheelset was equipped with a strain gauge-based telemetry system [8], developed for acquiring stress spectra based on a rainflow count processing of measured strain data. In addition, the OOR of the instrumented wheelset has been measured on regular occasions to quantify the evolution of tread damage.

In parallel, by employing the procedure described in Ref [14], an in-house software for the simulation of vertical wheel–rail contact forces and dynamic axle stresses for prescribed combinations of wheel–rail surface damage and vehicle operating conditions has been applied. For traffic on tangent track, the simulations were performed using the measured wheel OOR combined with different levels of rail roughness as input to a model of the vehicle–track system.

2. Field tests

In this chapter, the telemetry system, the instrumented train and the procedure used for the monitoring of bending stresses in the wheelset axle are described. Further, results from the measurements of wheel OOR are presented.

2.1. The telemetry and on-board data acquisition system

SmartSet® is a patented system developed by Lucchini RS for long-term monitoring of bending and torsion stresses at a specified section of an axle [8]. The strain data, which are processed on-train, are stored in the form of rainflow count data in a matrix of pre-defined combinations of intervals of mean values and amplitudes. The rainflow data are computed according to the guidelines given in Ref [15] and uploaded to a server when the train is at stand-still or when it passes a given GPS position. The data can later be analysed using a crack-growth algorithm, such as the one presented in Ref [16].

The SmartSet® system consists of strain gauges and a telemetry transmitter installed on the axle body, as well as of a telemetry receiver, a telemetry inductive power supply and an embedded data acquisition computer installed in the bogie or on the vehicle body. The system is designed to be capable of autonomously performing data acquisitions over several years, and it is powered by the train power supply. Figure 1 shows the studied powered wheelset before it was installed under one end of the studied bi-directional train.

The telemetry module on the axle is powered via an induction power head installed on the gearbox frame that induces a high-frequency alternating current in the inductive coil installed on the axle just below, see Figure 1. The telemetry module acquires data from four strain gauge full-bridges and processes the signals according to the rainflow count algorithm before storing the data in matrices (one matrix per strain gauge). The matrices are transmitted by telemetry to an on-board PC module by means of a 2.4 GHz radio connection. The strain gauges were placed 80 mm from the wheel seat, where the effect of the stress concentration near to the wheel seat fillet radius is negligible. In the present installation, two telemetry modules (each consisting of two full strain gauge bridges) were
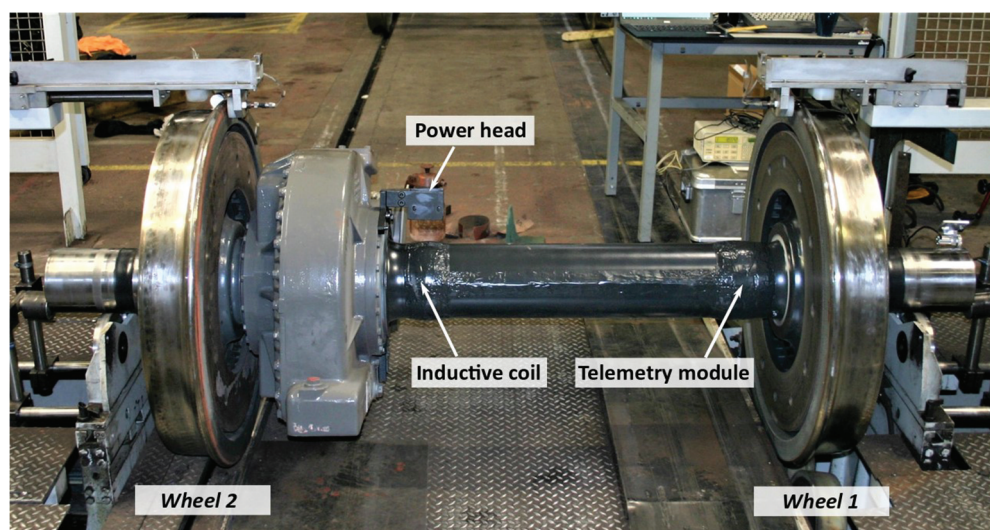
Figure 1. The instrumented wheelset before installation on the regional train. The strain gauges positioned at 80 mm from the wheel seat are part of the telemetry module.

installed so that axle bending stresses could be monitored at regular angular intervals of 45 degrees (0º, 90º, 225º and 315º). Here, it is assumed that each strain gauge bridge is capable of detecting the mean value and amplitude of the bending strain along one diametrical line of the axle cross-section. A sketch of the strain gauge configuration is shown in Figure 2(a). The telemetry system and the strain gauges are appropriately protected against the rough environmental conditions and impacts with external objects.

The on-board PC module stores the rainflow matrices from the telemetry system and transfers the data to a remote server by means of a GSM antenna on the external side of the train, see Figure 2(b). Data upload is normally activated by an automatic procedure based on GPS coordinates but can also be manually triggered by a remote user. Normally, GPS coordinates of train stations are stored directly in the PC module and used for triggering of data upload based on the current train position.

The rainflow matrices contain the cumulative spectra detected by the four strain gauges. These spectra are stored according to the prescribed combinations of amplitudes and mean values of the digital recordings coming from the strain gauge amplification circuit. The digital signals, which are measured in terms of an electrical signal ranging from −32,000 to +32,000 digits, are transformed to stresses by multiplication with a coefficient that depends on the geometry and elastic properties of the wheelset, and that has been calibrated during the installation of the telemetry system onto the axle. The downloading of matrices at specific GPS locations allows to relate measured stress spectra to traffic on specific sections of the network. This means that it is possible to assess the influence of track quality on measured axle stresses for each specified section of track. Moreover, stress spectra collected at different times of the year can be used to investigate the effect of seasonal variations (such as if there is a variation in track stiffness between winter and summer) or the effect of performed maintenance (such as the influence of a decrease in running surface roughness after wheel reprofiling or rail grinding).
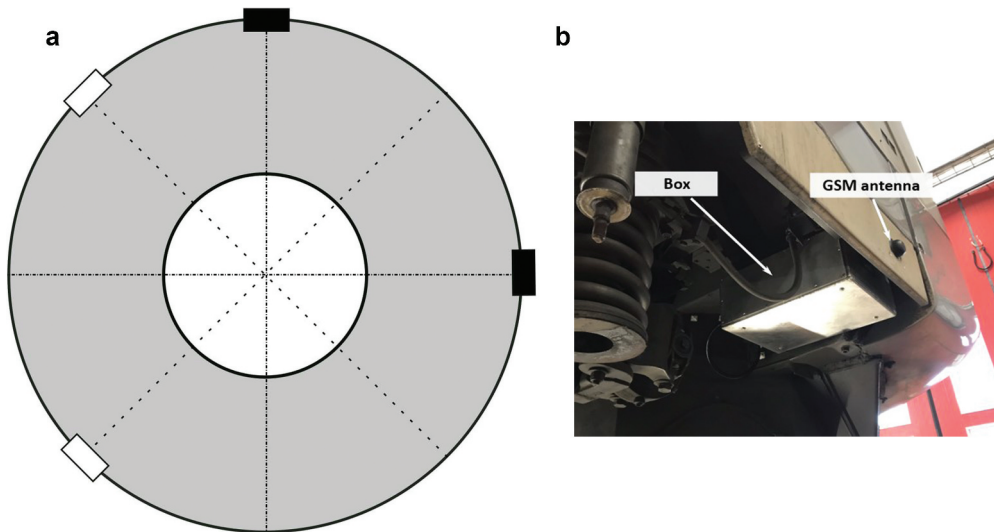
Figure 2. (a) Cross-sectional view of the strain gauge configuration adopted in the current study. The strain gauges connected to telemetry module 1 are represented by black rectangles, while those connected to telemetry module 2 are represented by white rectangles. (b) The positions of the GSM antenna and of the enclosure (box) containing the PC and GPS modules.

2.2. The instrumented train

The instrumented train is an X40 train operated by SJ (a state-owned Swedish passenger railway company). It is an electric multiple unit (EMU) of type Coradia Duplex produced by Alstom. The X40 consists of two or three double-decker coaches depending on the passenger capacity required on the route. The train can operate in both running directions at a maximum speed of 200 km/h. The axle load of the leading powered wheelset is 18.25 tonnes when the train is empty. However, since the two ends of the train are mainly reserved for the driver and electric equipment, the static load on the leading axle is not varying significantly during operation.

2.3. Evolution of wheel tread damage

The status of the wheel tread surfaces of the instrumented wheelset has been monitored on regular occasions. OOR measurements were performed at specific rolling circles, located at specified lateral positions on the wheel tread. The status of the wheel treads was also visually inspected to check for RCF clusters, wheel flats or other types of discrete damage. The wheel profiles were measured to quantify the wheel wear. In order to increase the probability of evolving wheel OOR, RCF clusters or other forms of tread damage within the scheduled test period, the test started off with wheels with slightly worn treads, see Figure 3(a). The main aim of these measurements was to obtain wheel OOR data to be used as input in simulations of vertical wheel–rail contact forces and axle bending stresses using an in-house software. However, these data were also used to study the evolution of tread damage occurring during service operation over a test period of more than one year.
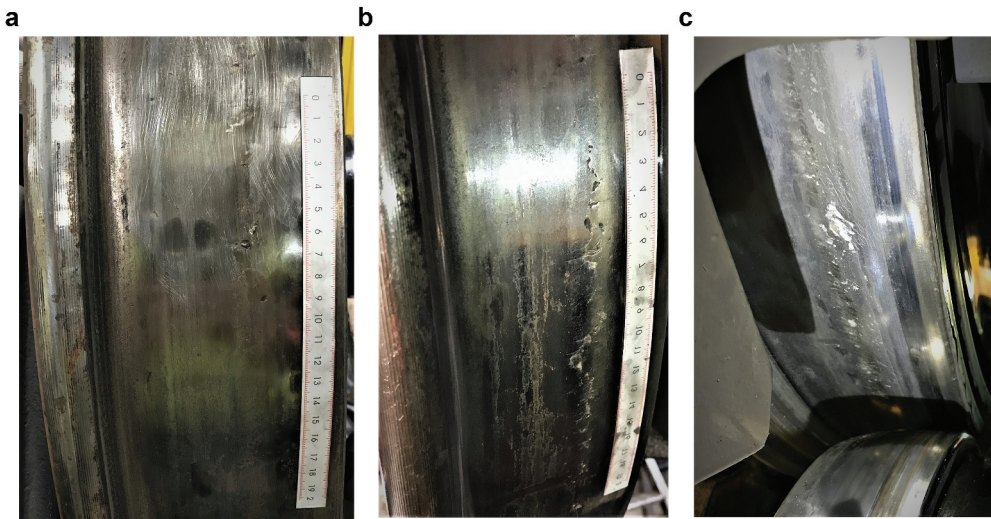
Figure 3. Evolution of wheel tread damage towards the field side of wheel 2. Pictures taken in (a) January, (b) March and (c) May 2019.

The wheel OOR was measured by an in-house measurement device. During the measurement activities, the wheelset was rotated manually after being lifted off the rail. A displacement probe with head radius R10 mm measured the radial deviation of the wheel tread surface around each selected rolling circle. At the same time, a pulse wheel kept track of the circumferential position. As sampling is time-triggered, the sampling rate depends on the speed at which the wheel is rotated. For the measurements presented in this work, the sampling distance varied between 4 and 6 mm, which was considered to be sufficient as the stresses measured by the instrumented telemetry were low-pass filtered at 500 Hz. For consistency, the stress time histories predicted by the simulation software have been post-processed using the same filter. At a vehicle speed of 130 km/h, this roughly corresponds to a sampling distance of 7 cm, which is significantly larger than the employed sampling distance. Further, using the same simulation model as the one of the present paper, it was shown in Ref [14]. that a wheelset bending mode occurring at frequency 206 Hz was dominating the dynamic axle bending stresses resulting from a wheel–rail impact due to a discrete wheel tread defect. Note that the measurements obtained using the in-house device have been validated against those obtained using a commercial equipment [17], which has displacement probes with a smaller head radius (R3 mm) and a constant sampling rate of 0.4 mm.

The first OOR measurement was performed on 25 January 2019, before the instrumented wheelset was mounted under the studied train. The wheelset was equipped with two worn wheels with a diameter of 864 mm. These wheels had previously been in traffic and already showed some minor RCF damage on the treads. The measurements were performed using the in-house device with the wheelset journals supported by rollers as shown in Figure 1. On both wheels, the OOR was measured at regular lateral intervals of 10 mm for rolling circles located between 25 mm and 85 mm from the wheel field side. In

this study, the wheel away from the gearbox is denoted wheel 1, while wheel 2 is the one near to the gearbox, see Figure 1.

The measurements were repeated in March 2019 (not shown here). In May 2019, the train with the instrumented wheelset was lifted in a maintenance depot in such a way that its primary suspension was compressed, effectively preventing undesired rigid motion of the wheelset that could interfere with the OOR measurement. The results obtained at some of the selected rolling circles from the measurements in January and May are compared in Figure 4. For both wheels, the comparisons show that the OOR has increased over time. In general, the OOR from May 2019 shows a larger range between peaks and troughs than the OOR from January 2019. Moreover, Figure 4(a,b) shows that clusters of discrete defects have developed on the tread towards the field side of both wheels. The geometry of the smallest wheel tread defects might not have been fully captured by the measurement equipment. However, because of the contact filter effect, where the wheel trajectory is not influenced by small defects (independent of their depth) since the wheel and rail surfaces make contact around the defect, the influence of these defects on wheel–rail contact forces and axle stresses can be expected to be negligible. Indeed, the parameter study presented in Ref [14]. showed that the increase in dynamic axle stresses due to a discrete defect with length 20 mm is negligible.

Figure 4(a,b) shows the OOR evolution at 45 mm from the field side of the wheel. In terms of peak-to-trough value, the ovality on both wheel treads has deteriorated from 60 μm to 100 μm. The overall shape of wheel 1 appears to be oval as two global maxima and two minima are visible at the nominal rolling circle, see Figure 4(c). Between January and May 2019, it is observed that the peak-to-trough of the ovality at the nominal rolling circle has grown from about 70 μm to 120 μm. Wheel 2 is instead characterized by a different form of OOR without a growth of ovality, see Figure 4(d). The peak-to-trough value of the OOR at the nominal rolling circle of wheel 2 has increased from 70 μm to 110 μm. Figure 4(e,f) shows the OOR measured 75 mm from the field side of the two wheels. Again, it is seen that the OOR on both wheels has increased in severity: the ovality of wheel 1 is more evident (a peak-to-trough increase in OOR from 50 μm to 110 μm), while the OOR of wheel 2 seems to have completely changed in shape. This last observation was confirmed by the measurements made at the rolling circle located 85 mm from the field side (not shown here).

The evolution of RCF clusters around the rolling circle located 45 mm away from the field side of wheel 2 between January and May 2019 is shown in Figure 3. In Figure 3(a), some small cracks are visible towards the field side of the wheel tread as well as a few small round-shaped indentations. Figure 3(b) shows that, between January and March, cracks have formed a network and RCF defects have grown on the tread. In May 2019, some of the RCF clusters have grown into larger defects, see Figure 3(c). During the same period, some minor surface cracks have grown on the tread of wheel 1, as well as some RCF defects (not shown here). However, the latter are less frequent and less deep than those on wheel 2.

2.4. Tread profile

The lateral profile of both wheel treads was measured in January, March and May 2019 using the commercial equipment MiniProf [18]. Wheel profiles measured on different occasions have been compared under the assumption that no wear occurs at the tip area of the flange.
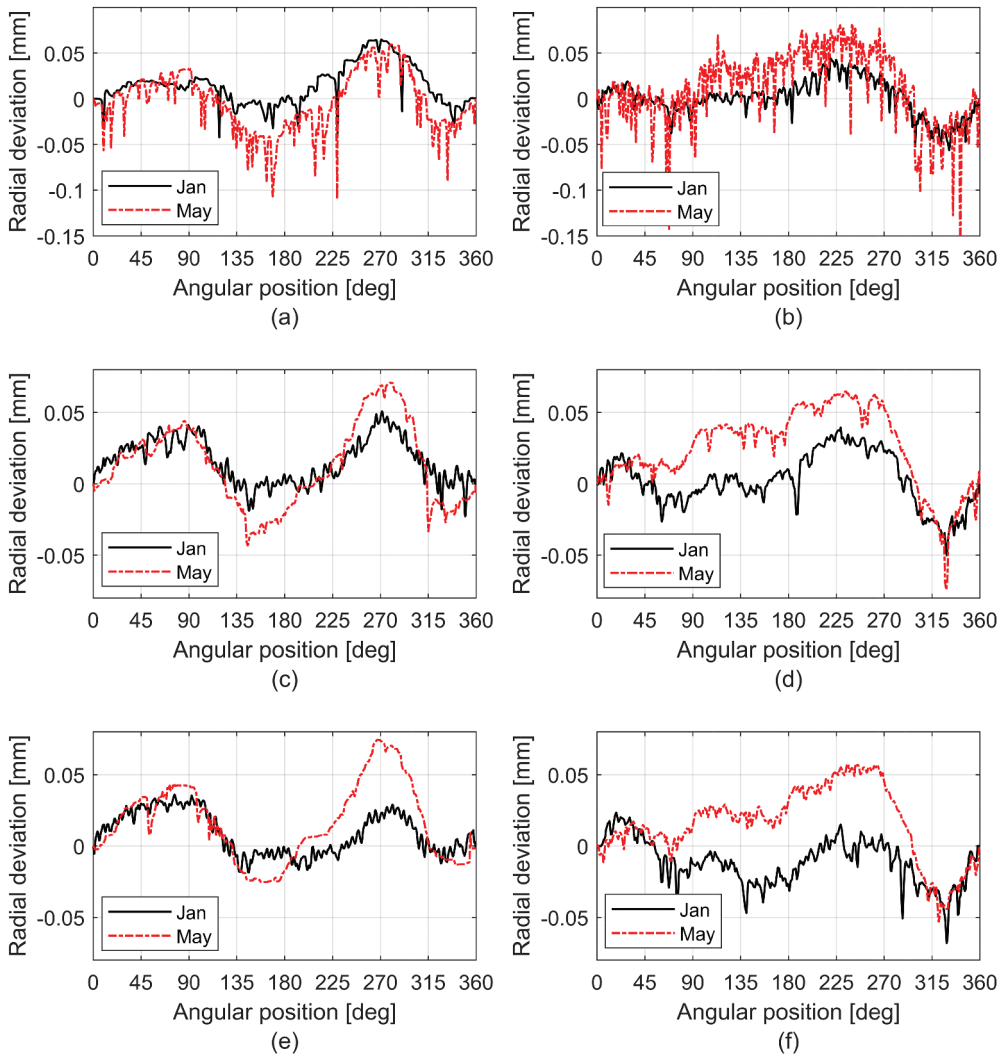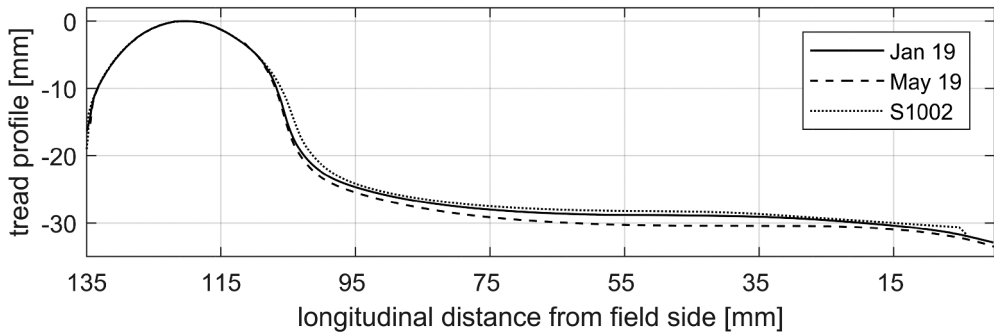
Figure 4. Measured OOR in January and May 2019. Plots are for rolling circles located at (a) and (b) 45 mm, (c) and (d) 65 mm (nominal rolling circle) and (e) and (f) 75 mm from the wheel field side. (a), (c) and (e) OOR on wheel 1, (b), (d) and (f) OOR on wheel 2.

In Figure 5, it can be seen that the radial wear at the nominal rolling circle is more than 1 mm between January and May. In comparison with the nominal S1002 wheel profile, a radial wear of 2 mm can be observed. Comparable wear patterns were obtained when wheel profiles were measured at other sections on both wheels. The tread profiles plotted in Figure 5 have been used to estimate the lateral positions of contact during curving, see Section 4.1.

3. Simulation model

A versatile and cost-efficient method to simulate the vertical dynamic interaction between a wheelset and railway track, accounting for generic distributions and shapes
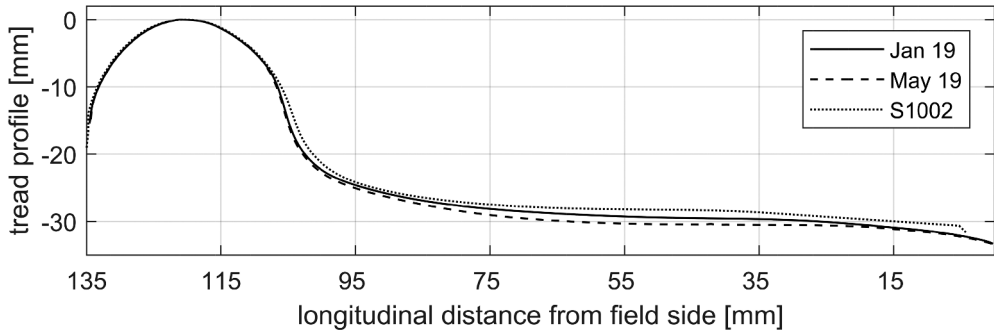
Figure 5. Lateral tread profiles for (a) wheel 1 and (b) wheel 2 measured in January and May 2019, and compared with the nominal S1002 wheel profile.

of wheel tread damage, has recently been presented in Ref [14]. The wheelset (comprising two wheels, axle and any attached equipment for braking and power transmission) and track with two discretely supported rails are described by three-dimensional finite element (FE) models. The simulation of dynamic vehicle–track interaction is carried out in the time domain. Time-variant stresses are computed for the locations in the wheelset axle which are prone to fatigue.

The wheelset model with the positions of the nodes where stress time histories have been computed is shown in Figure 6. It is based on the design of the powered wheelset mounted under one end of the X40 train. The geometry of the gearbox is approximated as a hollow cylinder with a mass of 200 kg under the assumption that 40% of the whole gearbox weight is borne by the axle. The wheels are modelled with a worn diameter of 864 mm and the web mounted brake discs are included. Each axlebox is modelled as a reference point with an inertial mass of 208 kg located at the centre of the journal. Each primary suspension is connected to a rigid reference and to the wheelset at the axlebox reference point. The wheelset model with 106,600 degrees of freedom (dofs) is meshed using twenty-node quadratic brick elements referred to as C3D20 in Ref [19]. More information about the material properties and the meshing technique is given in Ref [14].
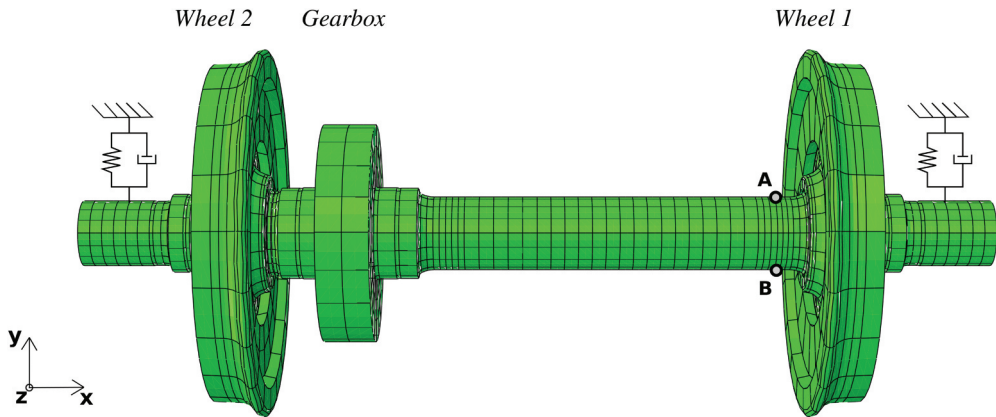
Figure 6. FE model of the instrumented wheelset. Stress time histories have been computed at nodes A and B.

The 3D periodic FE model of a tangent ballasted track section has been established in Abaqus using Python scripts. The mass, stiffness and damping matrices generated by the FE software are imported to a Matlab software, where the frequency response functions for the track are calculated. Only the vertical track dynamics is considered. The constant sleeper spacing is 0.60 m and the distance between the two rails is 1500 mm. Input data to the track model are listed in Ref [14]. Each sleeper is modelled as a uniform Rayleigh-Timoshenko beam that has been discretized using 20 elements of equal length. Each rail is modelled as a Rayleigh-Timoshenko beam with a discretization of eight elements per sleeper bay.

The complex-valued (including information about both magnitude and phase) frequency response functions are calculated at both contact points of the wheelset model, where the contact points are specified according to whether the wheelset is in tangent track or curved track, see Section 4.1. Once a receptance has been calculated, the corresponding Green's function is calculated by means of an inverse Fourier transform. A different mathematical formulation is necessary for the track since the relative motion between the wheelset and the track has to be accounted for. In a first step, ordinary Green's functions are computed from the direct and cross-receptances at several track positions to capture the response of the track up to a sufficient distance from the contact point. For a given train speed in the second step, samples from the set of ordinary Green's functions are combined to form the discrete moving Green's functions for the track.

The applied in-house MATLAB software for the simulation of dynamic vehicle–track interaction WERAN, which was originally presented in Refs. [20] and [21], solves the normal contact problem using the active set algorithm proposed by Kalker [22]. At the interface between the two bodies, a potential contact area is defined and discretized into a mesh of rectangular elements. In each time step, the elements that are in contact and their contact pressures are determined through an iterative procedure. The total vertical contact force acting between wheel and rail is computed by summing the contributions from the contact pressure values in all elements of the contact patch. The forces at the two contact patches are convoluted with the respective Green's functions to obtain the wheel

and rail displacements. The iteration proceeds to the next step when the displacements agree with the kinematic constraints listed in Ref [14].

Based on the calculated wheel–rail contact forces, time-variant stresses at critical locations in the wheelset are calculated in a post-processing step. The applied formulation is based on pre-computed stress frequency response functions, which are transformed into stress Green's functions by means of inverse Fourier transforms. The time history for the bending stress in the studied point is determined by convoluting the time histories of the contact forces at the two wheel–rail contact points with the respective stress Green's functions.

4. Results from field measurements and simulations

In this chapter, different scenarios of traffic on tangent track are simulated using the in-house software. Axle stresses are computed at the locations where the strain gauges are positioned and compared with the measured stresses under similar conditions.

4.1. Lateral contact position and out-of-roundness evolution

As described in Section 3, the in-house software for the simulation of vertical wheel–rail contact forces and axle stresses only considers the vertical dynamic interaction. However, the prescribed lateral position of the wheelset centre on the track, and consequently the lateral positions of the contact points on the wheel treads, will have an influence on the calculated axle stresses. The influence of longitudinal and lateral wheel–rail contact forces on the axle stresses is neglected.

The measured wheel profiles that were shown in Figure 5 have been used as input to the commercial multibody simulation software Simpack [23] to compute the influence of lateral wheelset displacement (relative to the track) on the lateral positions of the wheel–rail contacts, see Table 1. Track gauge 1435 mm and rail inclination 1:30 were used in the calculations. The 60E1 rail profile was assumed to be unworn.

According to Table 1, in January with no lateral wheelset displacement, the nominal rolling circle on wheels 1 and 2 was at approximately 75 mm and 55 mm from the field side, respectively. However, because of tread wear, the contact position on wheel 2 was shifted between January and May. In Figure 3, it was observed that RCF damage was particularly severe at 45 mm from the field side of wheel 2. According to Table 1, this corresponds to a contact position of approximately 85 mm from the field side of wheel 1. Based on the difference in rolling radius between the two wheels, it can be shown that this situation corresponds to radial steering in a curve with a radius of about 500 m. This case,

Table 1. Calculated lateral positions of contact on the two wheels and change in rolling radius. Numerical values are given in millimetres.

Running case	Tread profile measurement	Contact position from field side		Offset from nominal rolling radius	
		wheel 1	wheel 2	wheel 1	wheel 2
Tangent track	January 2019	75	55	−0.4	0.7
	May 2019	75	75	0.8	0.8
Curved track	January 2019	85	45	1.8	−0.7
	May 2019	85	45	2.3	−0.6

which is referred to as 'Curved track' in Table 1, was studied using the measured OOR at these rolling circles. As the aim of the simulations for the case of 'Curved track' is to assess the influences of the evolution of wheel OOR and the lateral shift of the wheel–rail contact points on vertical contact forces and axle stresses without considering any other effects due to curving, only the vertical dynamic interaction of the vehicle–track system has been accounted for. The effects of lateral wheel–rail contact forces and the redistribution of vertical loads between the inner and outer wheel during curving have been neglected.

To obtain a three-dimensional representation of the wheel surface, the measured wheel irregularities from January and May were post-processed by linear interpolation in the lateral direction using data from the different rolling circles. Further, for each rolling circle, the measurements were interpolated (re-sampled) to obtain a constant resolution in the longitudinal direction. An approximation of a large section of the measured wheel tread surface could thus be provided as input to the wheel–rail contact formulation in the simulation, using a resolution of 1 mm in both the lateral and longitudinal directions. Depending on the simulated load case, the contacts were centred on their respective rolling circles according to Table 1. The influence of rail roughness was also included in the contact model. For the simulations presented in this section, a sample of a rail roughness profile based on the spectrum specified in ISO 3095 [24] with wavelengths in the range 1–100 cm was used, see Section 4.2. The rail roughness profile had a lateral and longitudinal resolution of 1 mm.

All the simulations of wheel–rail contact force featured in this paper were performed for train speed $v=$ 130 km/h and axle load 18.25 tonnes. For the four cases in Table 1, the wheel–rail contact forces and axle stresses were calculated over a distance of 1 km, which roughly corresponds to 370 wheel revolutions and the passing of 1650 sleeper bays.

Figure 7(a) shows a section of the calculated contact force time history for the case with the measured wheel OOR from May 2019 and the lateral contact positions referred to as 'Tangent track'. For comparison, Figure 7(b) illustrates the case with the OOR measured on the same occasion but with contact positions corresponding to 'Curved track'. It is observed that the situation where wheel 2 is running on its most damaged rolling circle leads to a significant increase in high-frequency dynamics and higher maximum and lower minimum contact forces.

The calculated time histories of wheel–rail contact forces corresponding to the four cases listed in Table 1 have been used as input to a post-processing of axle bending stresses, see Ref [14]. The stress frequency response functions were extracted at the top and bottom nodes on the (non-rotating) axle circumference at the lateral position where the telemetry strain gauges were positioned in the field test, see nodes A and B in Figure 6. To account for the influence of axle rotation at a constant train speed v, the evaluated stress amplitude is calculated as

$$S(t) = \frac{\left(S_x^A - S_x^B\right)}{2} \cdot \cos\left(\frac{2vt}{d} + \varphi\right) \tag{1}$$

where S_x^A and S_x^B are the calculated bending stresses at nodes A and B and d is the wheel diameter. The position of node A with respect to the origin of the OOR measurements is accounted for by the angle φ (in radians). The simulations in Sections 4.1 and 4.2 are for
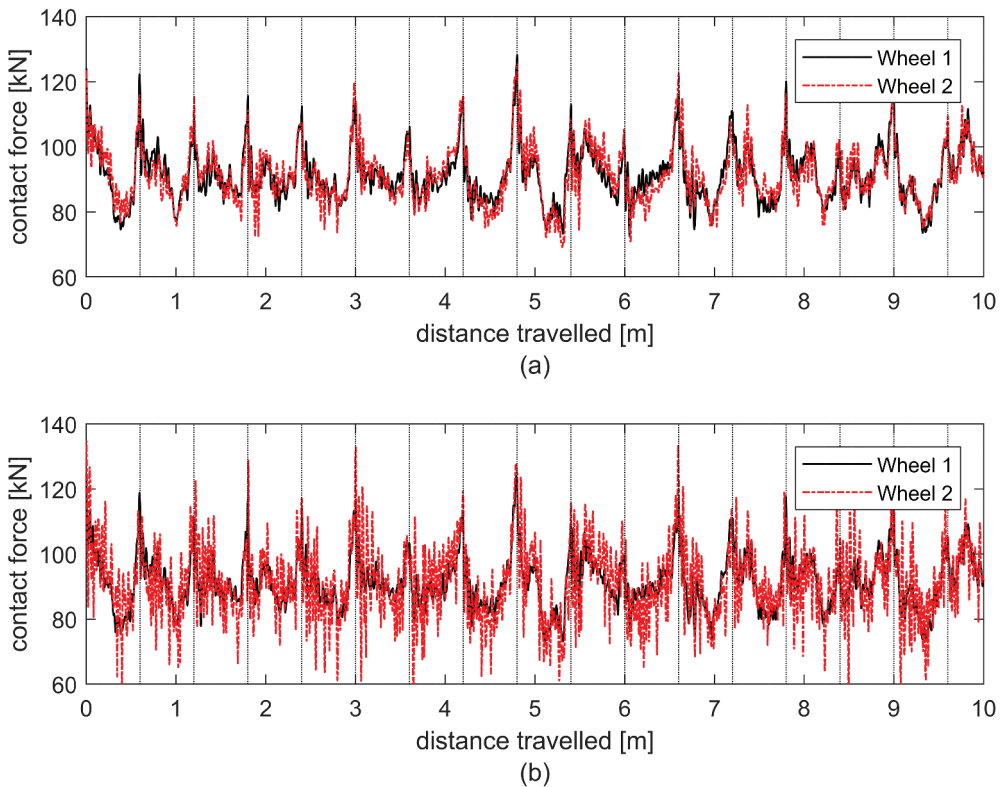
Figure 7. Calculated vertical wheel–rail contact forces: (a) 'Tangent track' and (b) 'Curved track' (R = 500 m). Wheel OOR measured in May 2019 and rail roughness based on the ISO 3095 spectrum.

$\varphi = 0$, while the influence of the angle is investigated in Section 4.3. Torsional stresses transmitted by the gearbox or the brake discs have been neglected, as all simulations have been performed at a constant speed of 130 km/h. Modifications in the stress field due to the shrink-fitting of wheels on the axle have been disregarded since they modify the mean stresses only and not the stress amplitudes.

The time history of the rotating bending stress $S(t)$ is low-pass filtered using a fourth-order Butterworth filter with cut-off frequency 500 Hz. This is meant to replicate the effect of the telemetry RC low-pass filter on the stresses measured by the strain gauges. An example of a simulated time history of rotating bending stress is plotted in Figure 8.

In a subsequent step, the filtered stresses have been post-processed using a rainflow count algorithm based on the method developed by Endo, as described in Ref [25]. The procedure adopted by the ASTM standard E1049 [15] and used by the telemetry PC is based on the same algorithm. The algorithm allows to compute the mean stress and the stress amplitude for each stress cycle. The effect of lateral wheel–rail contact forces due to curving or due to the negotiation of switches and crossings can alter the mean stresses. However, since lateral forces have not been accounted for in the simulations, the mean stresses are close to zero. The simulation results will thus be presented only in terms of stress amplitudes per cycle. Moreover, to facilitate the comparison of results obtained from train rides and/or simulations of different running distances, the results have been
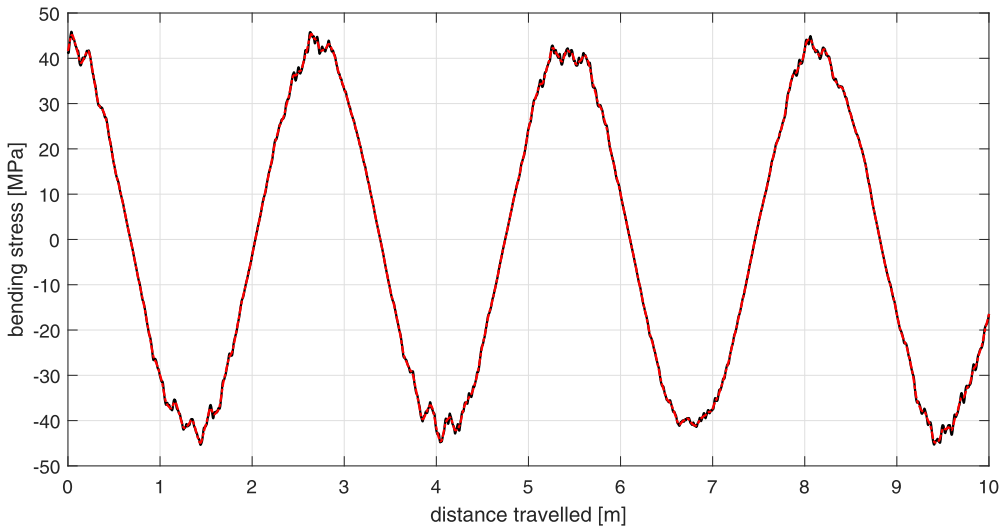
Figure 8. Calculated axle bending stress for the case of running on tangent track (to be consistent with the measured data, a low-pass filter at 500 Hz has been applied). Wheel OOR measured in January 2019 and rail roughness based on ISO 3095 spectrum. The non-filtered bending stress history is plotted in solid black line, while the low-pass filtered version is plotted in dashed-dotted red line.

normalized and plotted in terms of 'cycle ratio'. This expression indicates the ratio between the number of cycles falling within a given stress amplitude bin and the total number of cycles measured or simulated for a given train ride.

Based on simulation of the four cases in Table 1, the results from the evaluation of the number of cycles at different stress amplitudes are presented in Figure 9(a,c). An increase in the number of cycles at higher stress amplitudes can be observed for the cases representing 'Curved track' compared with the cases for 'Tangent track'. Further, the simulations employing OOR from May 2019 lead to an increase in the number of cycles at higher stress amplitudes compared with the simulations reflecting the OOR in January 2019. Note that cycles with amplitudes lower than 20 MPa have been excluded since they are not important for axle life and to be consistent with the measurement post-processing.

In Figure 9, it is observed that the influence of wheel tread condition on the shift of stress amplitude spectra is relatively weak. The increase in simulated stresses between tangent track in Figure 9(a) and curved track in Figure 9(c) is due to the combined effect of a modified wheel OOR and a lateral shift of the wheel-rail contact points away from the nominal rolling circle (see Table 1). To assess which of the two contributions that has a more significant effect on the increase in axle stresses, a fictitious 'Intermediate case' was introduced and studied, see Figure 9(b). In this case, the wheelset model was considering the contact position for traffic on tangent track, while the OOR was adopted according to the proper rolling circles in Table 1. It is observed that the stress amplitudes do not increase significantly between Figure 9(a,b), while the curves are shifted by about 1 MPa towards higher amplitudes between Figure 9(b,c). Thus, it is concluded that the increase in stress response due to the shift of the contact point has a larger influence on
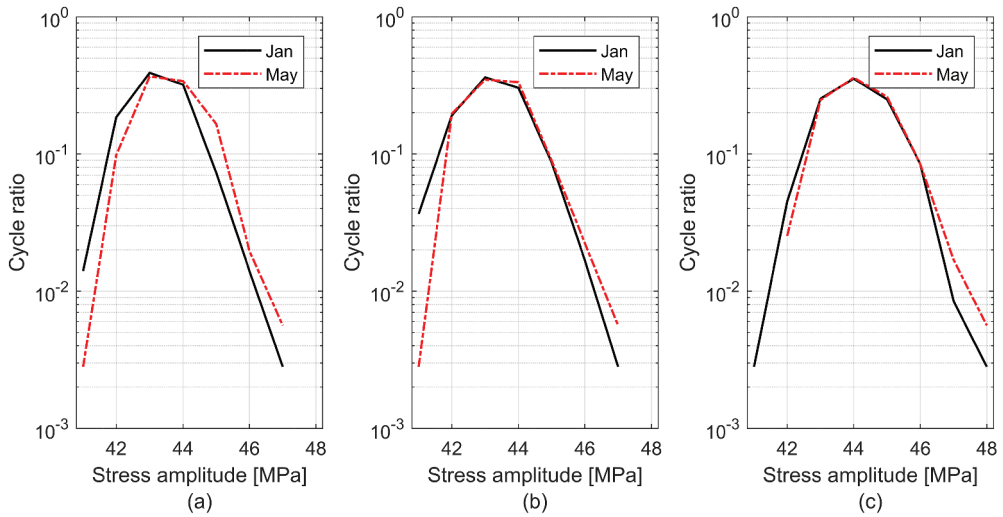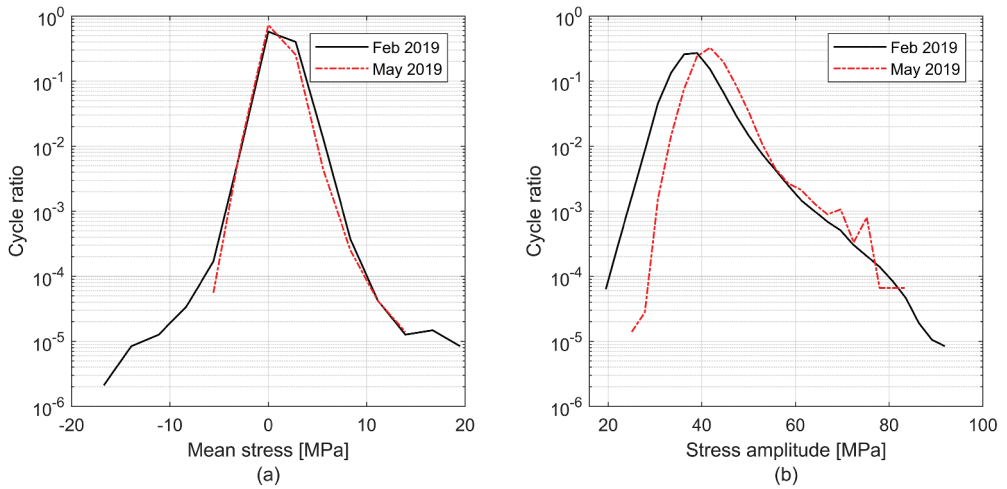
Figure 9. Simulated ratio between number of cycles at different stress amplitudes versus the total number of cycles for the cases (a) 'Tangent track', (b) 'Intermediate case' and (c) 'Curved track' (R = 500 m) and using OOR measured in either January 2019 or May 2019. Rail roughness based on the ISO 3095 spectrum.

the axle bending stresses than the deterioration in wheel OOR between January 2019 and May 2019.

The calculated increase in stress amplitudes due to the vertical wheel–rail interaction between the cases 'Tangent track' and 'Curved track' in May 2019 is around 2%, whereas the increase in peak contact forces is around 11%, see Figure 7. Thus, the increase in stresses does not reflect more than about 20% of the increase observed in the calculated vertical peak contact forces. It is argued that the damping and inertia of the wheelset assembly lead to an attenuation of the high-frequency contribution to the axle stresses. A similar trend was observed in the studies presented in Ref [14].

To investigate the effect of the 500 Hz low-pass filter implemented in the telemetry system, the simulation procedure was repeated for unfiltered stresses for the four cases in Table 1. For the same simulated time history of axle-bending stress, it was found (not shown here) that the stress amplitudes increased by between 0.5 MPa and 1 MPa if the filter was not applied, manifested as a corresponding shift of the entire stress amplitude spectrum. This increase is deemed negligible with respect to the overall stress amplitudes and thus the low-pass filtered time histories are employed throughout the present work.

The results in Figure 9 can be compared with the measurements from the telemetry system. The results acquired on the section of track from Örebro to Västerås on 21 February 2019 and on 16 May 2019 are shown in Figure 10. Stress cycles with amplitudes lower than 20 MPa have been neglected, as spurious oscillations in the voltage supply may be registered as low stress amplitude cycles by the telemetry system. During both journeys, the instrumented wheelset was in the leading position of the train. Figure 10(b) shows that the stress amplitudes shifted towards higher values from February to May 2019, where the most common loading changed from around 39 MPa to around 42 MPa. Measured mean stresses corresponding to the plotted amplitudes are between −20

Figure 10. Measured ratio between number of cycles at different (a) mean stresses and (b) stress amplitudes versus the total number of cycles. The data sets were measured by the telemetry system for one journey from Örebro to Västerås in February 2019 and May 2019.

MPa and +20 MPa, but the mean stresses pertaining to the most common amplitude cycles are normally close to zero, see Figure 10(a). The measured stress amplitudes occurring most frequently are slightly lower than the simulated ones, but overall there is good agreement between simulation and measurement. The small discrepancy may depend on several reasons, such as simplifying assumptions in the simulation model, uncertainty in assumed traffic conditions, or the calibration of the telemetry system before the field tests. Some cycles with higher stress amplitudes are captured during the field test. These can be due to curving in small radius curves or the negotiation of switches or crossings, which cause lateral contact forces on the wheelset that have a significant influence on the measured stresses.

4.2. Rail roughness level

In Section 4.1, one sample of a rail roughness profile based on the spectrum defined in the ISO 3095 standard [24] (extrapolated up to centre wavelength 1 m) was used. To mimic more representative conditions for general Swedish tracks, rail roughness at higher levels have been derived using the methodology described in Ref [26] by uniformly adding 3 dB or 6 dB to the ISO 3095 spectrum. The new samples of rail roughness profiles were generated based on a superposition of sine functions, see Equation (2). For each of the given number N of wavelengths λ_{ij} in each 1/3 octave band i, the amplitude a_i of the sine function is determined by the ISO 3095 spectrum, while the phase φ_{ij} is taken as random.

$$r(x) = \sum_{i=1}^{M} a_i \left[\sum_{j=1}^{N} \sin\left(\frac{2\pi}{\lambda_{ij}} x + \varphi_{ij} \right) \right] \quad (2)$$

In the summation, M 1/3 octave bands with centre wavelengths λ_i ranging between 1 cm and 100 cm have been accounted for. At train speed 130 km/h, these wavelengths

correspond to excitation in the frequency interval 36–3611 Hz. The *N* wavelengths in each band *i* were determined by assuming a constant wave-number increment [26].

From the simulations employing the OOR from May 2019, the influence of rail roughness level on the vertical wheel–rail contact forces is shown in Figure 11. For the case of running on a relatively smooth rail (roughness according to ISO 3095), the highest peaks in the contact forces reach approximately 120 kN. If 3 dB or 6 dB is added to the roughness spectrum, the peak forces increase to about 130 kN or 150 kN, respectively.

To further investigate the requirements on rail surface quality to enable detection of wheel tread damage, time histories of wheel–rail contact force for different combinations
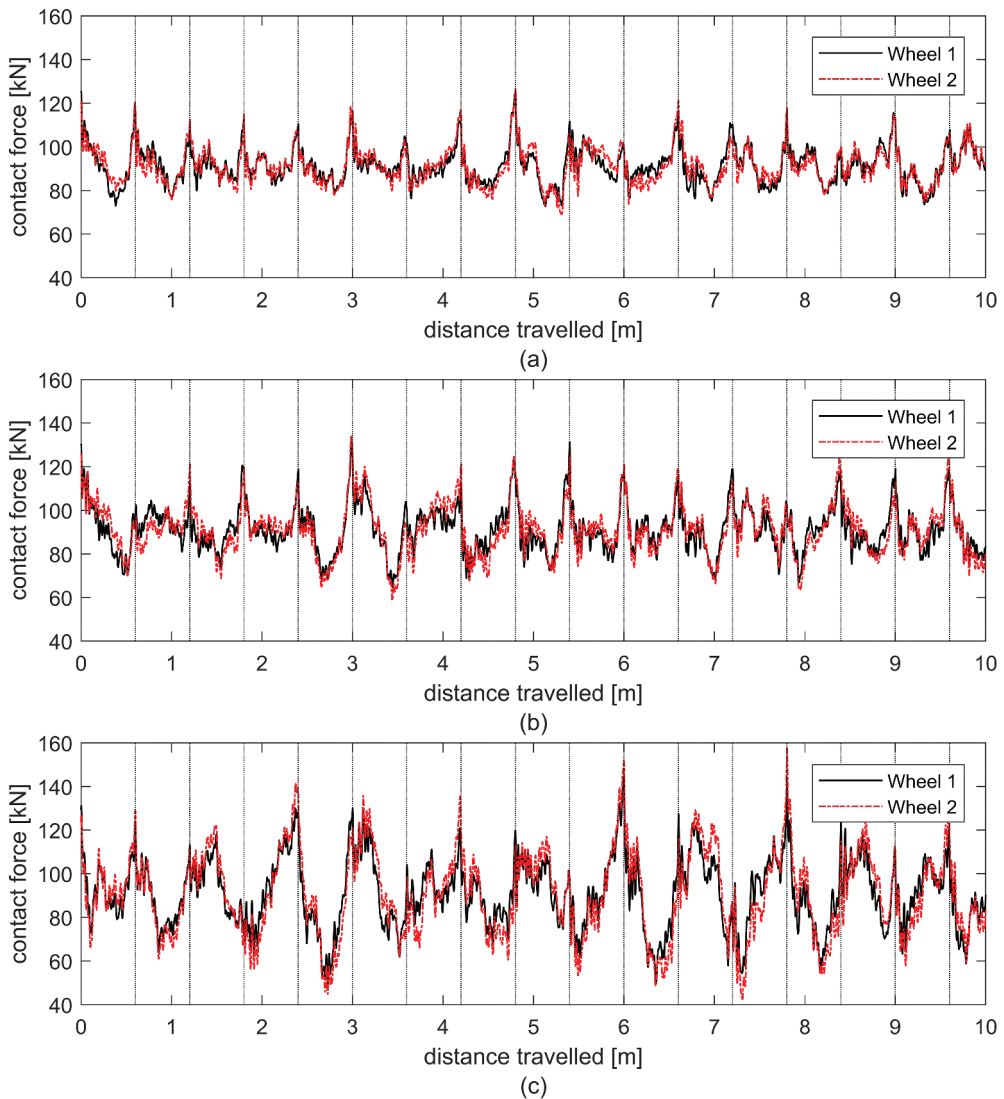
Figure 11. Simulated vertical wheel–rail contact forces for the case of 'Tangent track' with wheel OOR measured in May 2019. Samples of rail roughness profiles derived from (a) ISO 3095 (b) ISO 3095 + 3 dB (c) ISO 3095 + 6 dB.

of wheel OOR and levels of rail roughness have been calculated for a track section of about 1 km in length. Using the procedure described in Section 4.1, the corresponding time histories of bending stress in the axle have been computed and the rainflow count procedure has been applied.

The results in terms of the number of cycles at different stress amplitudes are plotted in Figure 12. The highest detected stress amplitudes when rail roughness is neglected are in the order of 44 MPa for the wheel OOR of January 2019 and 45 MPa for the OOR of May 2019, while the stress amplitudes increase to 49 MPa (independently of the adopted wheel OOR) if 6 dB is added to the ISO 3095 irregularity spectrum. However, for all the studied cases in Figure 12 it is also visible that the majority of the simulated amplitudes still fall in the bins around 44 MPa. This shows that an increase in rail roughness level generates a noticeable increase in the maximum simulated stress amplitudes generated in the axle, but the stress amplitude for the most common loading is not affected as much. Between the case in which no rail roughness is prescribed and the case in which the roughness spectrum from ISO 3095 is increased by 6 dB, the average stress amplitude
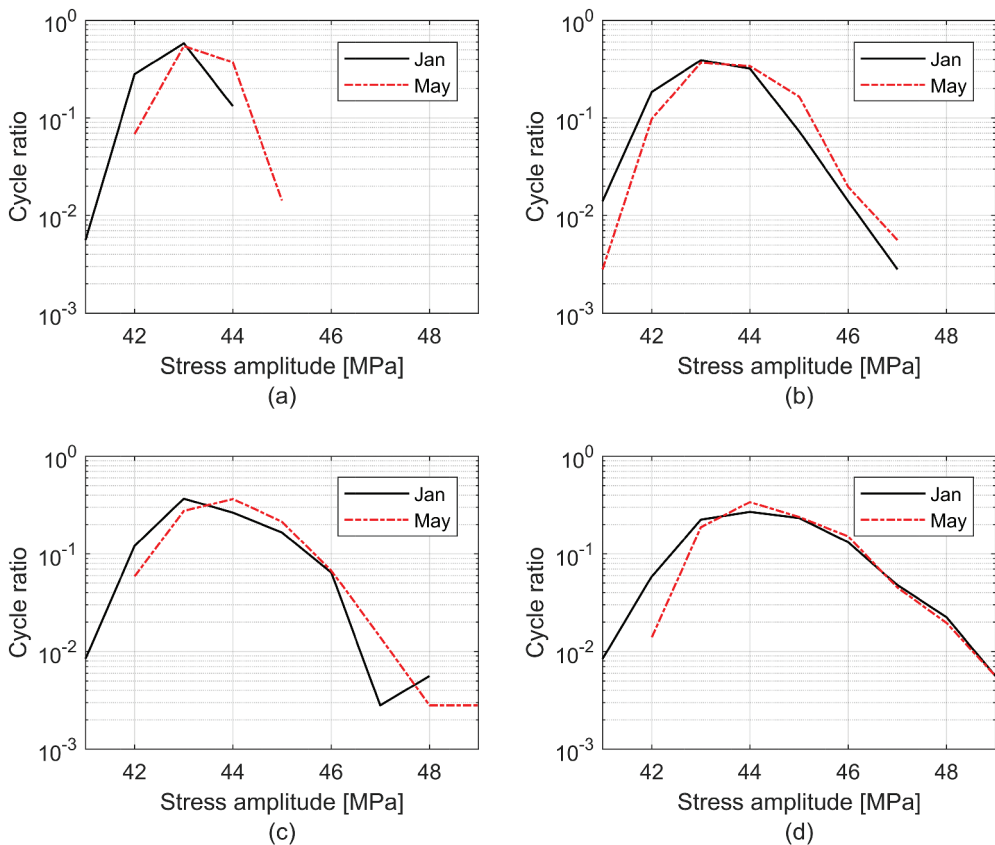

Figure 12. Simulated ratio between number of cycles of with different stress amplitudes for the case 'Tangent track'. OOR measured in either January 2019 or May 2019 with (a) neglected rail roughness, or rail roughness according to (b) ISO 3095 (c) ISO 3095 + 3 dB (d) ISO 3095 + 6 dB.

increased from 43.4 MPa to 44.9 MPa for the simulations performed using the OOR from January 2019 and from 43.8 MPa to 45.1 MPa when applying the OOR from May 2019.

Furthermore, Figure 12 shows that for the simulated rail roughness spectra used in subfigures (a) to (c), it is possible to detect a shift towards higher amplitude values due to the degradation of the wheel tread surface between January and May 2019. In Figure 12 (d), on the other hand, the difference between the two curves at higher amplitudes is negligible. Thus, for these particular samples of wheel tread damage, these results indicate that if the spectrum of rail roughness level is equal to or exceeds the ISO 3095 + 6 dB, the measured axle stresses would be more affected by the level of rail roughness than by the degradation of the wheel tread. This sets a limit for the applicability of the present sensor arrangement in terms of requirements on track quality.

In the static calculation of axle stresses according to the standard EN 13103–1 [4], the applied vertical wheel loads should be multiplied with a factor 1.25 to account for the dynamic loading. The maximum normalized wheel load has been computed using the OOR from January 2019 and different rail roughness level spectra. The ratio between the maximum simulated bending stress amplitude and the static value of the axle bending stress according to FE calculations (41.5 MPa) was also computed for the same cases. The results are shown in Figure 13. It can be concluded that, although the maximum dynamic wheel–rail contact forces may exceed the static wheel load by 70% (and possibly more if severe discrete defects are present on the wheel tread, see [14]), the magnification factor 1.25 adopted in the standard seems to be a realistic approximation for the expected increase in axle stresses due to dynamic excitation in the field. As observed in Figure 13,
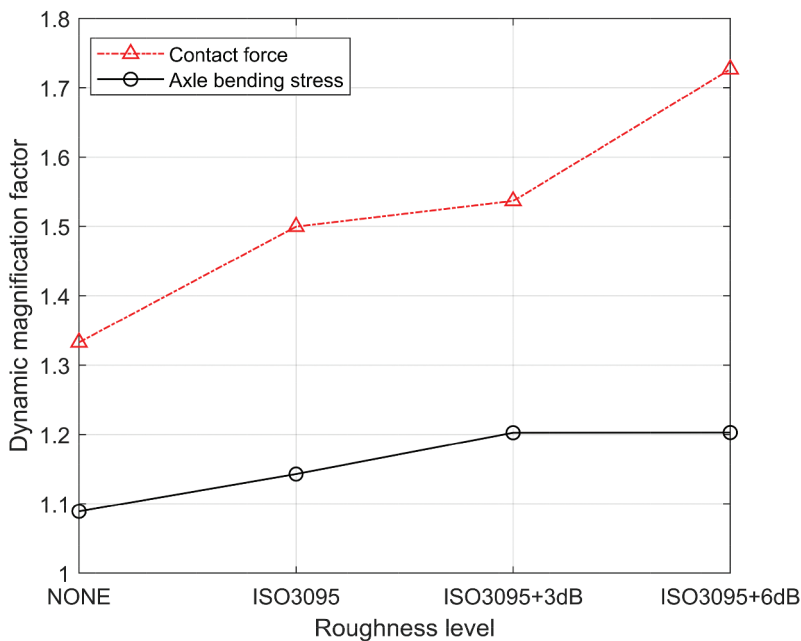
Figure 13. Maximum values of computed wheel–rail contact forces and axle stresses normalized by their static value for different levels of rail roughness. Wheel OOR from January 2019.

the dynamic magnification is in the order of 20% for the case with a rail roughness level according to the ISO 3095 spectrum increased by 6 dB.

4.3. Strain gauge position

In this section, the influence of the angular positions of the strain gauges on the axle relative to the origin of the measured OOR (0º in Figure 4) is investigated by simulation. The aim is to assess whether significant differences in stress amplitudes would be captured by the different measurement channels, corresponding to different angular strain gauge positions, if the tread damage is not uniform around the wheel circumference.

The studied configurations relate to the case 'Tangent track' in Table 1. The wheel OOR from either January or May 2019 and a rail roughness profile based on the ISO 3095 spectrum were used in the simulations. Bending stress amplitudes $S(t, \varphi)$ have been computed for phase angles φ in the interval 0º to 360º at regular intervals of 2.5º, see Equation (1). In order to allow for an easier comparison with the results registered by the telemetry system, simulated stress amplitudes are visualized by histograms with bin width 2.75 MPa.

To highlight the ability of the telemetry system to capture variations in the stress spectra, the percentage of cycles that fall into the most common stress ranges are studied in detail. To this end, the relative occurrence of the two bins collecting amplitudes between 41.25 MPa and 44 MPa and between 44 MPa and 46.75 MPa are shown in Figure 14 as a function of the angular position of the point where the stresses were assessed.
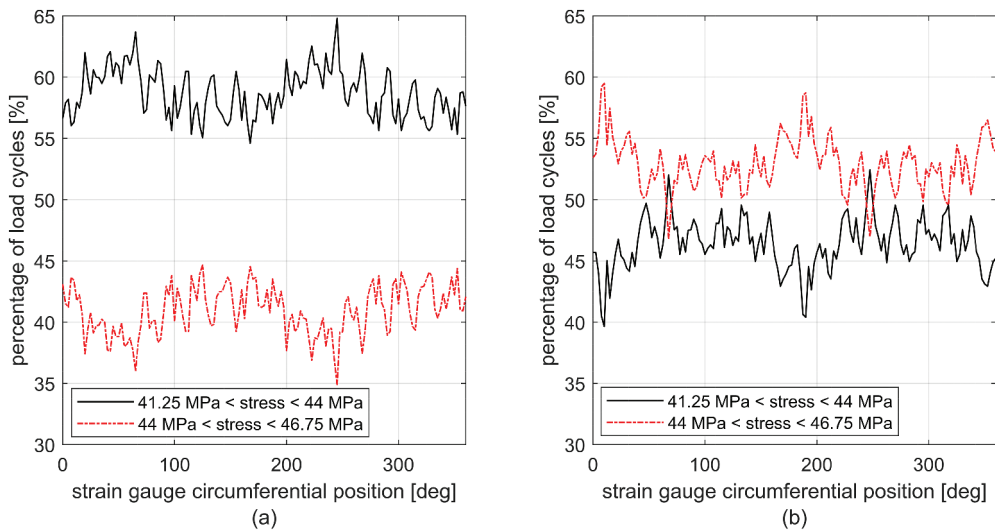
Figure 14. Simulated ratio of number of cycles in the two most common stress amplitude intervals versus the total number of simulated cycles. The ratios are plotted as a function of the simulated strain gauge position relative to the origin of the OOR measurements. Rail roughness according to ISO 3095 and OOR measured in (a) January 2019 and (b) May 2019.

The graphs show that the relative occurrence of simulated stress amplitudes for the most common bins depend on the angular position of the strain gauge bridge and that it varies by up to 11 percentage points for the OOR of January 2019 and by 10 percentage points if the OOR from May 2019 is used. An interesting finding is that an increase in the occurrence for the most common bin is compensated for by a corresponding decrease in the second most common bin and vice versa. For the OOR considered here, this means that a different angular position of the strain gauge has the potential to make a stress cycle transfer from one stress bin to a neighbouring one. A further investigation of the influence of strain gauge position is presented in [27].

Note that the OOR measurements showed that the wheels in the instrumented wheel-set were characterized by an ovality and by the presence of RCF defects that were uniformly distributed along the tread surface on the field side of each wheel, cf. Figure 3. It was found (not shown here) that these defects did not generate a significant increase in axle stresses from a fatigue point of view depending on the locations of the strain gauges neither in the measurements nor in the simulations. For a more local discrete wheel tread defect, this situation can be expected to be different.

5. Conclusions

Based on a convolution integral approach to represent the dynamics of wheelset and track, a method for the simulation of dynamic vehicle–track interaction has been applied to quantify the influences of the evolution of wheel OOR, the lateral position of the wheel–rail contact and the level of rail roughness on generated wheel–rail contact forces. For different scenarios, the influence of the evolution of wheel tread damage on the calculated bending stress at a specified location in the axle has been evaluated. The results were compared to those measured in a field test using a wheelset instrumented with a telemetry system. For the studied contribution of vertical loading on axle bending stress spectra, good agreement between simulations and measurements was observed. Simulations have also been carried out for cases that could not be controlled during the field test to investigate the influences of variations in rail roughness level and the positions of the strain gauges. It was shown that variations in rail roughness level may lead to a significant influence on axle stresses, which may supersede the influence of the degradation of wheel OOR and generated RCF clusters.

The influence of the angular position on the axle where stresses are monitored with respect to the wheel OOR has also been investigated. For the wheel tread damage measured on the instrumented wheelset, both the results from the simulation and the field test show that, from a fatigue point of view, the variation in bending stress amplitudes was not significantly affected by the measurement position. In future work, the influence of other forms of wheel damage on stresses measured at different angular positions can be studied. For example, it can be expected that the influence of a wheel flat generating large periodic variations in axle strain would be most easily captured if the strain gauge was located directly above the location where the flat hits the rail. Significant differences in the stress amplitudes measured by different strain gauge positions could then be expected.

The good agreement between field test measurements and computed bending stress amplitudes shows that the results from the simulation software are reliable. The evolution

of computed stress amplitudes due to the degradation of the wheel tread surface can be used as input to predictions of fatigue life using a suitable high-cycle fatigue criterion or a crack growth algorithm. Based on such results, the planned maintenance can be scheduled to an earlier or later occasion. Priority can be given to trains where the monitored stresses of some components are more critical. This allows for a more efficient use of resources for the train operator, as well as for more flexibility in the usage of the fleet.

Acknowledgments

Disclosure of potential conflicts of interest

No potential conflict of interest was reported by the author(s).

Funding

References

[1] Bracciali A. Railway wheelsets: history, research and developments. Int J Railway Technol. 2016;5:23–52.
[2] Zerbst U, Klinger C, Klingbeil D. Structural assessment of railway axles – a critical review. Eng Fail Anal. 2013;35:54–65.
[3] Pieraccini S; [cited 2017 Jan 31]. Strage di Viareggio, la ricostruzione di un disastro con 32 vittime [Viareggio accident, the reconstruction of a disaster with 32 victims]. Il Sole 24 Ore. Available from: https://www.ilsole24ore.com/art/strage-viareggio-ricostruzione-un-disastro -32-vittime–AEdJKPL
[4] European committee for standardization (CEN). Railway applications – wheelsets and bogies – part 1: design method for axles with external journals. Brussels: CEN; 2017. Standard No. EN 13103–1:2017.
[5] Watson AS, Timmis K. A method of estimating railway axle stress spectra. Eng Fract Mech. 2011;78:836–847.
[6] Carboni M. Reliability of non-destructive testing in the railway field: common practice and new trends. In: Prabhakar VV, Raghu VP, Narendra SJ, editors. Risk based technologies. Singapore: Springer; 2019. p. 173.
[7] European committee for standardization (CEN). Railway applications – in-service wheelset operation requirements – in-service and off-vehicle wheelset maintenance. Brussels: CEN; 2017. Standard No. EN 15313:2016.

[8] Cantini S, Cervello S, Regazzi D, et al. Optimization of in-service UT inspection intervals based on wheelset loads monitoring - SMARTSET®. Proceedings of the XIX International Wheelset Congress (IWC2019); 2019 Jun 16–20; Venice, Italy. p. 6.

[9] Ben-Daya M, Kumar U, Prabhakar Murthy DN. Condition-based maintenance. In: Ben-Daya M, Kumar U, Prabhakar Murthy DN (Eds.), Introduction to maintenance engineering: modeling, optimization and management. New York (USA): John Wiley & Sons Ltd; 2016. p. 355–387.

[10] Maglio M, Asplund M, Nielsen JCO, et al. Digitalisation of condition monitoring data as input for fatigue evaluation of wheelsets. Proceedings of the XIX International Wheelset Congress (IWC2019); 2019 Jun 16–20; Venice, Italy. p. 5.

[11] Available from (2021, May 31): https://www.skf.com/my/industries/railways/solutions/insight-rail

[12] Bracciali A, Cavaliere F, Macherelli M Review of instrumented wheelset technology and applications. Proceedings of the Second International Conference on Railway Technology; 2014 Apr 8–11; Ajaccio, France. p. 16.

[13] Gullers P, Andersson L, Lunden R. High-frequency vertical wheel–rail contact forces – field measurements and influence of track irregularities. Wear. 2008;265:1472–1478.

[14] Maglio M, Pieringer A, Nielsen JCO, et al. Wheel–rail impact loads and axle bending stress simulated for generic distributions and shapes of discrete wheel tread damage. J Sound Vib. 2021;502:116085.

[15] American Society for Testing and Materials International (ASTM International). Standard practices for cycle counting in fatigue analysis. USA: ASTM; 2017. standard E1049 – 85.

[16] Beretta S, Carboni M, Cantini S, et al. Application of fatigue crack growth algorithms to railway axles and comparison of two steel grades. Proc Inst Mech Eng J Rail Rapid Transit. 2004;218:317–326.

[17] Available from (2015, May 28): Triceratops – Circumferential Wheel Irregularity Measurement. https://www.railway-technology.com/products/triceratops/

[18] Available from (2021, May 31): https://greenwood.dk/railway/instruments/miniprof-bt-wheel/

[19] Simulia A. User guide. France: Dassault Systemes; 2018.

[20] Pieringer A, Kropp W, Thompson DJ. Investigation of the dynamic contact filter effect in vertical wheel/rail interaction using a 2D and a 3D non-Hertzian contact model. Wear. 2011;271:328–338.

[21] Pieringer A, Kropp W, Nielsen JCO. The influence of contact modelling on simulated wheel/rail interaction due to wheel flats. Wear. 2014;314(1–2):273–281.

[22] Kalker J. Three-dimensional elastic bodies in rolling contact. Dordrecht (The Netherlands): Springer; 1990.

[23] Simulia S. Documentation. France: Dassault Systemes, 2020; 2021.

[24] International Organization for Standardization (ISO). Acoustics — railway applications — measurement of noise emitted by railbound vehicles. Geneva: ISO; 2013. Standard No. 3095:2013.

[25] Dowling NE, Kampe SL, Kral MV. Fatigue of materials: introduction and stress-based approach. In: Mechanical behavior of materials: engineering methods for deformation, fracture, and fatigue. 5th ed ed. Harlow (United Kingdom): Pearson; 2019. p. 375–449.

[26] Nielsen JCO. Numerical prediction of rail roughness growth on tangent railway tracks. J Sound Vib. 2003;267:537–548.

[27] Maglio M. Influence of wheel tread damage on wheelset and track loading – field tests and numerical simulations [Licentiate thesis]. Gothenburg (Sweden): Chalmers University of Technology; 2020.